JOURNAL OF AIRCRAFT
Vol. 37, No. 5, September–October 2000

# Hover Performance Prediction Using Full-Potential Method and Comparison with Experiments

E. Berton,* D. Favier,† and C. Maresca‡
*University of Aix–Marseilles I and II, 13009 Marseilles, France*

**A computational and experimental effort to investigate the flow around rotor blades in hover is presented. The experimental analysis of the flowfield in the immediate vicinity of the blade is supported by laser velocimetry (LV) performed on the three-dimensional velocity field around the blade section and in its near wake. A specific LV data processing method based on the momentum equation applied around a blade section has been developed to identify the contribution of the induced-drag component to the total sectional drag coefficient. From the computational approach, some improvements to a vortex embedding full-potential method are checked by direct comparisons with test data. Comparisons are performed for overall rotor airloads (thrust and torque coefficients), local sectional coefficients (lift and drag contributions), and flowfield characteristics, including the tip vortex path and the spanwise circulation distribution.**

## Nomenclature

| | | |
|---|---|---|
| $b$ | = | number of blades |
| $Cd$, $Cdt$ | = | drag coefficient of airfoil section |
| $Cdi$ | = | induced drag coefficient of airfoil section |
| $Cdp$ | = | profile drag coefficient of airfoil section |
| $Cl$, $Clt$ | = | lift coefficient of airfoil section |
| $C_Q$ | = | rotor power coefficient |
| $C_{Qi}$ | = | rotor induced-drag coefficient |
| $C_T$ | = | rotor thrust coefficient |
| $c$ | = | rotor blade chord, m |
| $\mathrm{d}Di$ | = | elementary induced-drag force, N |
| $\mathrm{d}F_{\mathrm{ex}}$ | = | external elementary forces, N |
| $\mathrm{d}F_x$ | = | horizontal elementary force, N |
| $\mathrm{d}F_z$ | = | vertical elementary force, N |
| $n$ | = | blade rotational frequency, revolutions per second |
| $P$ | = | static pressure, Pa |
| $\boldsymbol{q}^V$ | = | vortical velocity, m s$^{-1}$ |
| $R$ | = | rotor blade radius, m |
| $Ro$ | = | root cut out, m |
| $r$ | = | radial distance from the rotation axis, m |
| $T$, $Q$ | = | rotor thrust and torque, N, Nm |
| $U$, $V$, $W$ | = | radial, tangential, and axial velocities, m/s |
| $u$, $l$ | = | upper and lower side of the blade section |
| $\boldsymbol{V}$ | = | velocity vector |
| $V_e$ | = | rotational tip speed, $\Omega R$, m s$^{-1}$ |
| $\Gamma$ | = | blade circulation along the span, m$^2$ s$^{-1}$ |
| $\theta$ | = | collective pitch angle, deg |
| $\theta_V$ | = | blade twist law, deg |
| $\rho$, $\rho_\infty$ | = | density, kg m$^{-3}$ |
| $\sigma$ | = | rotor solidity, $bc/\pi R$ |
| $\psi$, $\psi_b$ | = | angular blade rotation, deg |
| $\Omega$ | = | angular rotational frequency, rad s$^{-1}$ |

## I. Introduction

ACCURATE prediction of hover performance is required for good rotor design. That is, it is necessary to accurately predict blade lift and drag distributions, and this capability is mainly a function of the ability to predict the rotor wake. This paper concerns the development of means to measure lift/drag distributions and to predict these using a free-wake computational fluid dynamics method.

To investigate drag mechanisms, previous experimental work[1–3] has been devoted to develop high-resolution laser velocimetry (LV) methods that are able to determine sectional loads' contributions to overall hover performance. Within this scope, an LV methodology has been specially developed to investigate the flow in the rotation plane, around the blade section and in its near wake. The so-called Kutta and momentum equation (KME) method and potential and momentum equation (PME) method have been derived for determining the lift and drag sectional coefficients along the blade span.

From the computational approach, a full vortex embedded potential method used in previous work[4–9] for the prediction of rotor hover performance is described, with emphasis on calculating the induced-drag contribution to the total sectional drag term. This numerical method has been implemented in a computer code, Phoenix II. In the present work, three major improvements have been made to this numerical method. As will be described, such improvements will concern specifically the modification of the trailed marker convection process within the computational grid, an optimization of the underrelaxation coefficients relative to the vortical velocity component, and an azimuthal extension of the velocity calculation domain, including the flow region close to the blade trailing edge.

The objectives of the present study are first to determine the blade sectional airloads by means of the momentum equation applied to the three-dimensional velocity field measurements provided by the LV methodology and then to assess the improvements given to the Phoenix II computational method by direct comparisons with experimental data.

## II. Experimental Methodology

The rotor is a model provided by the U.S. Army Aeroflightdynamics Directorate (AFDD) at NASA Ames Research Center and has been tested at the Institut de Recherche sur les Phénomènes Hors Equilibre/Laboratoire d'Aérodynamique Subsonique Instationnaire (IRPHE/ASI). The model-scale rotor was set up on the hovering test rig of the S1-Luminy wind tunnel. The test stand itself was mounted on an antivibration pad within the wind-tunnel test hall. The rotor configuration tested was a two-bladed, 2.13-m-diam teetering rotor with rectangular tip blades. The blades are of a stiff graphite composite construction designed to minimize aeroelastic deformations. Key geometric features of these blades are summarized in Table 1.

Several measurements techniques suited for surveying the flow in the near- and far-wake regions and around the blades have

Received 4 July 1999; revision received 1 March 2000; accepted for publication 7 March 2000. 

*Research Scientist, IRPHE/ASI Laboratory, Centre National de la Recherche Scientifique, 163 Avenue de Luminy, case 918. Member AIAA.

†Senior Research Scientist, IRPHE/ASI Laboratory, Centre National de la Recherche Scientifique, 163 Avenue de Luminy, case 918. Senior Member AIAA.

‡Senior Research Scientist, IRPHE/ASI Laboratory, Centre National de la Recherche Scientifique, 163 Avenue de Luminy, case 918. Associate Fellow AIAA.

**Table 1 AFDD one-seventh-scale rotor geometry**

| Property | Value |
|---|---|
| Number of blades | 2 |
| Rotor radius | 1066.8 mm (42.0 in.) |
| Inboard chord | 89.4 mm (3.521 in.) |
| Blade aspect ratio | 11.928 |
| Cutout | 0.28$R$ |
| Thrust-weighted solidity | 0.05027 |
| Twist distribution | |
| 0.28$R$ | 15.428 deg |
| 0.86$R$ | 8.72 deg |
| 1.0$R$ | 6.30 deg |
| Airfoil distribution | VR-12, 3-deg tab |

been developed at the IRPHE/ASI Laboratory[1–3] including X-wires anemometry and a long focal length (2 m) LV technique. Overall force measurements (averaged thrust and torque) are performed by means of a six-component balance mounted on the rotor hub. Tip vortex paths are measured by means of a hot-wire technique that allows the determination of the wake position as a function of the blade azimuth.

The three-dimensional velocity field around a blade section located at a spanwise station $r/R = \text{const}$ is measured by a high-resolution fiber-optic laser velocimeter system. In the vicinity of the blade, the velocity components $U$ and $V$ and the axial component $W$ are determined by LV in a fixed coordinate system. A glycerin-based smoke generator is used to seed the flow. The use of a 500-step encoder provides an azimuthal resolution of 0.72 deg. The velocity components are statistically averaged over 50–80 samples per azimuthal step ($\Delta\Psi = 0.72$ deg). The detailed characterization of the flowfield is made possible by a combination of the 0.1-mm step resolution afforded by the laser optics traverse and the 0.3 mm diameter of the LV system measuring volume. The initiation and synchronization of the instantaneous acquisition data are realized by means of a photocell delivering the azimuthal origin ($\Psi = 0$ deg).

Based on this LV methodology, two methods, KME and PME, have been derived to determine lift and drag sectional coefficients.

### A. KME Method for Local and Overall Airloads Determination

The KME method has been based on the application of the Kutta and momentum equations to a general control surface surrounding the blade section at a given radial station $r/R$. The KME method is described in detail in Refs. 1–3. Note that the specific approach used for the hovering flight case results from the periodicity of the velocity field along the vertical branches of the control surface extending between two consecutive blades (axisymetric flow). In this case, the elementary total drag force $\mathrm{d}F_x$ (see Fig. 1) can be deduced from the determination, as a function of the blade azimuth $\psi(0 \le \psi \le 2\pi/b)$, of the axial $W = W(\psi)$ and tangential $V = V(\psi)$ velocity components measured on the upper side and lower side of the airfoil section:

The momentum equation is

$$-\oint_{\Sigma_a} \mathbf{dF}_{\text{ex}}\,\mathrm{d}s = \oint_{\Sigma} P\cdot\boldsymbol{n}\,\mathrm{d}s + \oint_{\Sigma}(\rho\boldsymbol{q}\cdot\boldsymbol{n})\cdot\boldsymbol{q}\,\mathrm{d}s$$

$$-\mathrm{d}F_x = \rho r\int_0^{2\pi/b}[W_l V_l - W_u V_u]\,\mathrm{d}\psi$$

$$\Omega C = b\int_{R_0}^{R_1}\mathrm{d}F_x(\Omega r)\,\mathrm{d}r, \qquad C_Q = \frac{\Omega C}{\rho\pi R^2 V_e^3}, \qquad (V_e = \Omega R)$$

The circulation/Kutta equation is

$$\Gamma_r = \oint_{ABCD} V\,\mathrm{d}s = r\int_0^{2\pi/b}(V_l - V_u)\,\mathrm{d}\psi$$

$$\mathrm{d}F_z = \rho\Omega r^2\int_0^{2\pi/b}(V_l - V_u)\,\mathrm{d}\Psi, \qquad T = b\int_{R_0}^{R_1}\mathrm{d}F_z\,\mathrm{d}r$$

$$C_T = \frac{T}{\rho\pi R^2 V_e^2}$$

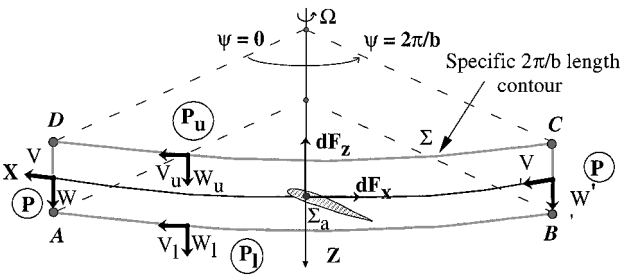


**Fig. 1 KME method in hovering flight configuration.**

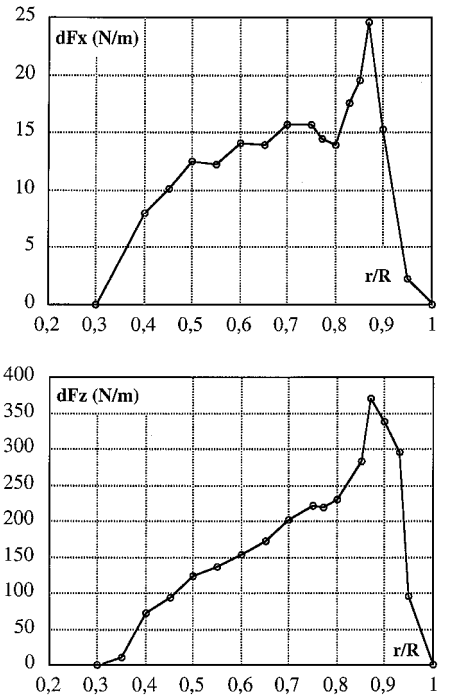


**Fig. 2 Spanwise elementary forces ($\mathrm{d}F_x$, $\mathrm{d}F_z$) distributions derived using the KME method: $\theta = 6$ deg and $\Omega = 125.7$ rad/s.**

where

$$\text{periodicity} \Rightarrow (p, V, W)_{AD} = (p, V, W)_{BC}$$

As shown in Fig. 1, the vertical lift component $\mathrm{d}F_z$ is deduced from application of the Kutta equation and the circulation measurement around a given radial section of the blade.

The overall thrust and power coefficients $C_T$ and $C_Q$ are deduced from the integration of the elementary forces $\mathrm{d}F_x$ and $\mathrm{d}F_z$ along the blade span as shown in Fig. 1. The sectional airloads coefficients $C_L$ and $C_D$ along the blade span are deduced from $\mathrm{d}F_x$ and $\mathrm{d}F_z$ using the flow streamlines and the blade element theory around the given blade section[1–3] to provide the local airfoil aerodynamic incidence $\alpha$.

An example of the results obtained on the present hovering rotor configuration from the use of a KME method along the blade span is given in Fig. 2 at the pitch angle value $\theta = 6$ deg. Overall thrust and power coefficients $C_T$ and $C_Q$ are, thus, obtained by integrating the elementary forces $\mathrm{d}F_x = \mathrm{d}F_x(r/R)$ and $\mathrm{d}F_z = \mathrm{d}F_z(r/R)$ distributions along the span. In Fig. 3, the results of the ($\mathrm{d}F_x$, $\mathrm{d}F_z$) integration along the span are compared with those deduced from direct overall measurements using the rotative balance, and the results show good agreement. The lift and drag linked to the local aerodynamic incidence $\alpha$ of the airfoil section are obtained by projecting, on the lift and drag axis, the elementary forces $\mathrm{d}F_x$ and $\mathrm{d}F_z$ measured by the KME-LV-based method.

### B. PME Method for Induced-Drag Determination

The method based on the PME applied to the bidimensional velocity field measured by LV around a given blade section is derived as follows.[10,11]

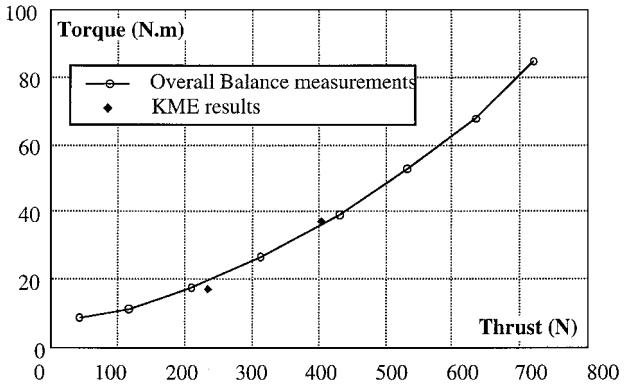


**Fig. 3 Comparison of integrated $dF_x$ and $dF_z$ distributions with global thrust and torque measurements.**

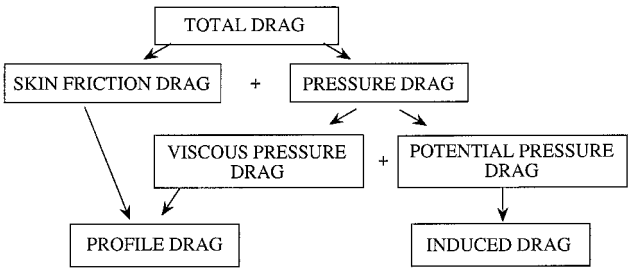


**Fig. 4 Total drag decomposition.**

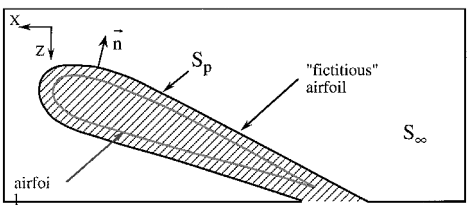


**Fig. 5 Momentum equation for general control surface around blade section.**

First consider the blade section an isolated airfoil; each contribution to the total drag $Cdt$ is split into two contributions: the profile drag $Cdp$ and the induced drag $Cdi$, as shown in Fig. 4. The viscous pressure effects and skin friction contribute to the profile drag $Cdp$, whereas the induced drag $Cdi$ can be considered the result of the pressure force contribution in the potential flow without the viscous effects contribution.

Based on such a total drag decomposition, it is assumed that viscous effects are significant only within the boundary layer and the near wake shed at the trailing edge section. Inside of this region, viscous effects appear as one of the sources of momentum responsible of the profile drag contribution $Cdp$. Outside this region, the potential flow appears as a source of momentum generating the induced-drag contribution $Cdi$.

The PME method is based on the application of the momentum equation to the control surface $S = Sp + S_\infty$ as shown in Fig. 5.

Here,

$$dDi = -\int_{S_p} P\boldsymbol{n}\,dS = \int_{S_\infty} P\boldsymbol{n}\,dS + \int_{S_\infty} \rho(|\boldsymbol{q}\cdot\boldsymbol{n}|)\boldsymbol{q}\,dS$$

Therefore, the periodicity of the flow generated in the specific case of hovering flight is used as shown in Fig. 6, and the elementary induced drag force $dDi$ resulting from the pressure forces acting on a fictitious airfoil of $Sp$ contour can be expressed as

$$dD_i = \int_0^{\Psi_1} W_1\cdot V_1\,d\Psi + \int_{\Psi_2}^{2\pi/b} W_1\cdot V_1\,d\Psi - \int_0^{2\pi/b} W_u\cdot V_u\,d\Psi \quad (1)$$

**Table 2 Uncertainty estimates**

| Measured quantity | Uncertainty (averaged value), % |
|---|---|
| Tip vortex path (hot-wire anemometry) | ±3 |
| Velocity field (laser Doppler velocimetry) | |
| Axial velocity $W$ | ±3 |
| Tangential velocity $V$ | ±3–5 |
| Overall airloads (rotative balance) | ±2 |
| Local airloads: lift and drag coefficients and circulation (velocity integration) | ±4–7 |

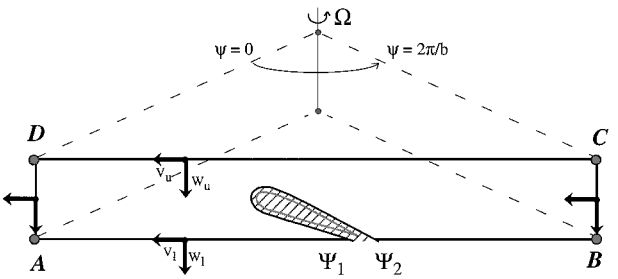


**Fig. 6 Momentum equation applied to $2\pi/b$ length-specific contour for hovering rotor.**

where $\Psi_1$ and $\Psi_2$ are the wake limits along the horizontal segment AB of the contour. These wake limits can be easily determined from the velocity profiles measured by LV on the lower side of the airfoil section as described in Refs. 10 and 11.

### C. Experimental Uncertainty Analysis

The measurement uncertainty analysis allows the separation and quantification of random and systematic errors in the different measurement methods implemented for the present study. These sources of error are due to the instrumentation itself, the geometric alignment and positioning of the laser beams, the model geometry inaccuracies, etc. Moreover, the KME and PME methods for local and global airloads determination introduce additional inaccuracies because forces and moments are obtained as a result of integrating the measured flow velocities. The estimation of all of these experimental uncertainties can be found in Refs. 1–3, 7, and 8. Specifically, for the LV method, the procedure is based on comparisons of measurements obtained from repeated runs and consists of a statistical estimate of variance of velocity measurements. In the same way, the uncertainty in the hot-wire measurements is estimated using the calibration data (the hot-wire probes are calibrated both before and after the data acquisition). Measurement uncertainties that quantify the deviations from averaged values are summarized in Table 2. Tip vortex path uncertainties concern radial $r/R$ and axial $z/R$ coordinates of the vortex referred to the blade radius $R$.

## III. Computational Method

One of the major tasks in helicopter rotor performance analysis is the accurate calculation of the rotor lift and power.[12,13] Typically, lift is found by surface pressure integration and is generally well predicted by finite difference methods when the induced inflow is well modeled. However, power depends directly on drag, which is very sensitive to small changes in surface pressure. The total drag is composed of two parts: induced drag and profile drag. Induced drag is the predominant hover drag mechanism and can account for nearly 75% of the total power. The sectional induced-drag coefficient is obtained by pressure integration for an inviscid flow.

The computational method used in the present study is based on the full potential equation with embedded vorticity regions.[4–9] This numerical method solves the compressible mass conservation equation and is coupled with an integral boundary-layer routine for power prediction. This method, implemented in Phoenix II, uses a vortex embedding (VE) scheme in potential flow. VE performs the convection of thin vortical regions, such as a hovering rotor wake,

using a Lagrangian wake tracking/relaxation method. This method differs from classic vortex-lattice methods because the velocity field is found using the mass conservation equation rather than the Biot–Savart law. Therefore, VE has the ability to compute both the free-wake evolution and the inviscid compressible flow on the blade with no geometric modeling limitations. Moreover, when combined with a boundary-layer solver, this provides the ability to predict hover performance with no need for initial prescribed wake or airfoil tables.

The numerical method is based on solving the steady mass conservation equation:

$$\nabla(\rho \boldsymbol{V}) = 0 \tag{2}$$

The total velocity $\boldsymbol{V}$ is split into an irrotational velocity field $\nabla\phi$ and a rotational velocity field $\boldsymbol{q}^V$:

$$\boldsymbol{V} = \boldsymbol{\Omega} \times \boldsymbol{r} + \nabla\phi + \boldsymbol{q}^V \tag{3}$$

The vortical part $\boldsymbol{q}^V$ is concentrated near the sheet and represents the trailed circulation. The term $\boldsymbol{\Omega} \times \boldsymbol{r}$ only results from rotational coordinate transformation. A fixed grid is used to solve the compressible potential flow equation to determine the potential $\phi$. To solve the potential equation, the density $\rho$ normalized by the corresponding freestream value takes the usual isentropic form away from the sheet:

$$\rho/\rho_\infty = \left\{1 - [(\gamma - 1)/2]M_\infty^2 [(\boldsymbol{\Omega} \times \boldsymbol{r})^2 - \boldsymbol{q}^2]\right\}^{1/(\gamma-1)} \tag{4}$$

The vortical component $\boldsymbol{q}^V$ is spread over several grid points around the vortex sheet to concentrate the vorticity.[4–6] The numerical method locates the trailed sheet by a Lagrangian convection of trailed circulation elements (markers). The circulation contained in these markers is then imposed on the flow as a $\boldsymbol{q}^V$ distribution (Clebsch type).[7–9] The solution process is an iteration between the convection of trailed markers (convection of the shed vorticity) and the solution to the potential equation (mass conservation). In the present numerical method a Nash–Macdonald boundary-layer scheme is implemented to compute the profile power. In this method, von Kármán's integral equation is solved for the momentum thickness. This accounts for weak viscous–inviscid interactions for an approximate determination of the skin-friction drag.

## IV. Results and Discussion

### A. Numerical Improvements

The numerical procedure modifications that have been provided to the Phoenix II prediction method are described here and detailed in Refs. 7 and 8. These modifications were first made and checked on a four-bladed rotor (ASI model 7), with aspect ratio of 15 ($R = 0.75$ m and $c = 0.05$ m), rectangular tip shape, tip Mach number of 0.40, and OA209 profile (9% thickness ONERA airfoil) and linear twist such that pitch increases by 8.3 deg from root to tip.

One major drawback of the numerical procedure was a trend of the markers to gather into the tip region and to be generally sparse in the other regions (a major cause of instability). In fact, it is very important for the numerical modeling to optimize the distribution of markers so that every grid cell encompassing the sheet contains at least one marker. Therefore, first improvement concerns the convection of the trailed markers within the computational grid. This has been done by modifying the numerical distribution of the markers below the rotor disk (code version Phoenix II-M). Figure 7 compares the results obtained from Phoenix II and Phoenix II-M code versions on thrust and power coefficients. The comparisons with the corresponding experimental data show an improvement of the numerical prediction on the rotor power coefficient when using the Phoenix II-M code version. It is also shown that the thrust and torque coefficients totally converge in nearly 20 iterations.

The comparison in Fig. 8 concerns calculation vs experiment on the circulation distribution along the blade span and on the tip vortex path. Note that the circulation peak is rather well predicted by the Phoenix II-M code version, but that the contraction of the wake $[r/R = r/R(\Psi)]$, however, is not sufficiently improved when compared to experiments. These discrepancies relative to the evolution

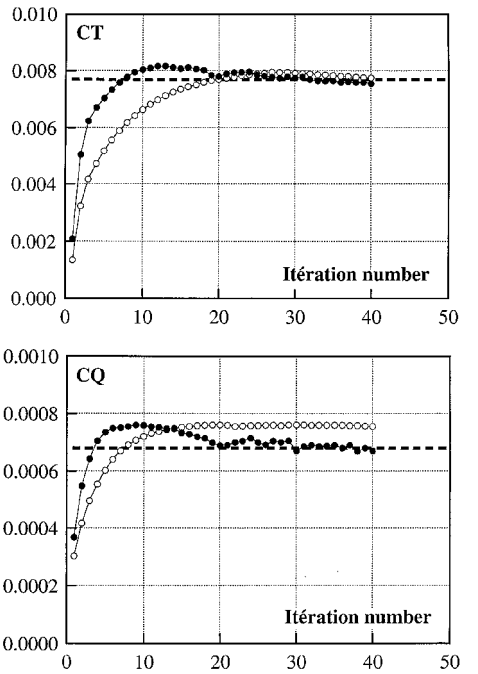


**Fig. 7 Computed overall *CT* and *CQ* performance histories: rotor ASI 7, four blades, and $\theta$ = 10 deg. - - - -, measurements; ∘, Phoenix II; and ●, Phoenix II-M.**

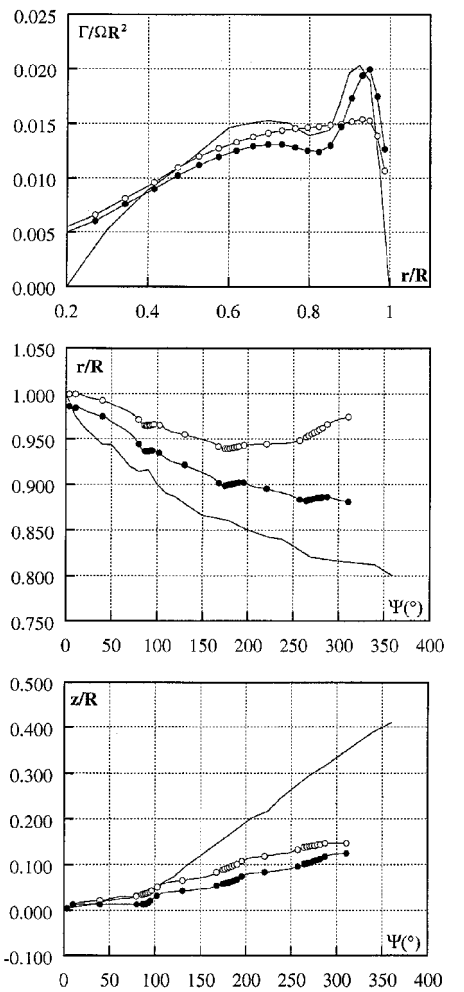


**Fig. 8 Circulation distribution, and radial and axial convection of the tip vortex: rotor ASI 7, four blades, and $\theta$ = 10 deg. ——, measurements; ∘, Phoenix II; and ●, Phoenix II-M.**

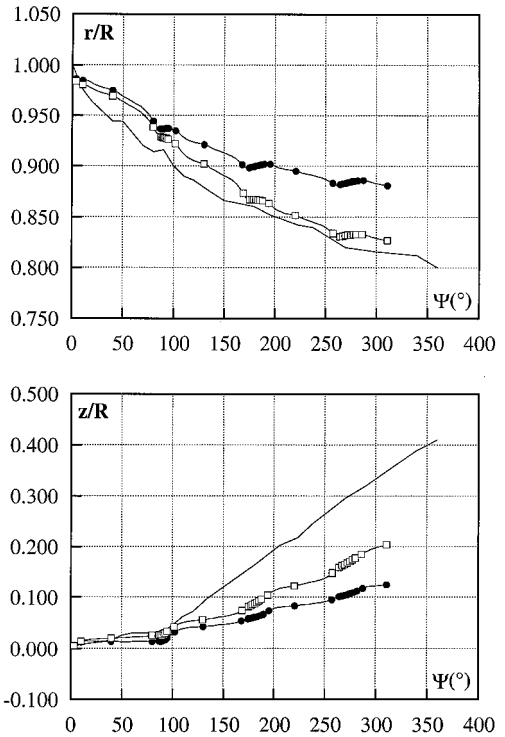


**Fig. 9 Radial and axial convection of the tip vortex: rotor ASI 7, four blades, and $\theta$ = 10 deg. ——, measurements; ●, Phoenix II-M; and □, Phoenix II-MV.**

of the vortex sheet are due to an underprediction of the vortical velocity $\boldsymbol{q}^V$ under the rotor disk, as revealed by the evolution of $z/R$ (Fig. 8), where no change in slope appears.

To overcome this problem, the second code improvement concerns modeling of the vortical velocity $\boldsymbol{q}^V$ for the entire azimuthal calculation domain including the blade–vortex interaction region at $\Psi = 90$ deg in the case of a four-bladed rotor (code version Phoenix II-MV). These modifications have improved the radial location of the tip vortices when compared to Phoenix II-M, as shown in Fig. 9.

The extension of the azimuthal domain is also of concern for the calculation of the axial velocity after the first blade–vortex interaction. The improvement consists of an increase of $\boldsymbol{q}^V$ based on the change in slope of $z/R$ (code version Phoenix II-MVL). The comparisons obtained with this final code version (Fig. 10) finally show good agreement with experimental data both in the circulation distribution and tip vortex path. However, there is still a tendency to underpredict the far-field axial convection rate.

### B. Numerical Uncertainty Considerations

The present numerical simulation of the flow involves two essential steps: the definition of a suitable mathematical model that describes the physical system and the development and implementation of numerical techniques to compute a solution of the mathematical model using computers. Both steps introduce necessary approximations in the simulation, and the resulting errors must be independently quantified. The validation of computational methods is not a simple comparison of numerical results with experimental data. It must be established that the mathematical model is logically consistent and that it is approximated by a correct numerical method, which is in turn implemented in a correct computer program.[14] Calculation runs are performed using a Cray YMP C90, without any special effort to vectorize the source code. A mesh refinement study has been conducted to ensure that there were not significant variations in the solution when either the number or the position of the mesh points is varied. A typical run using a fine enough mesh of about 240,000 grid points and about 40 iterations requires about 4-h CPU to complete the simulation. In our case, the major part of uncertainty concerns the geometric coordinates of the markers. The

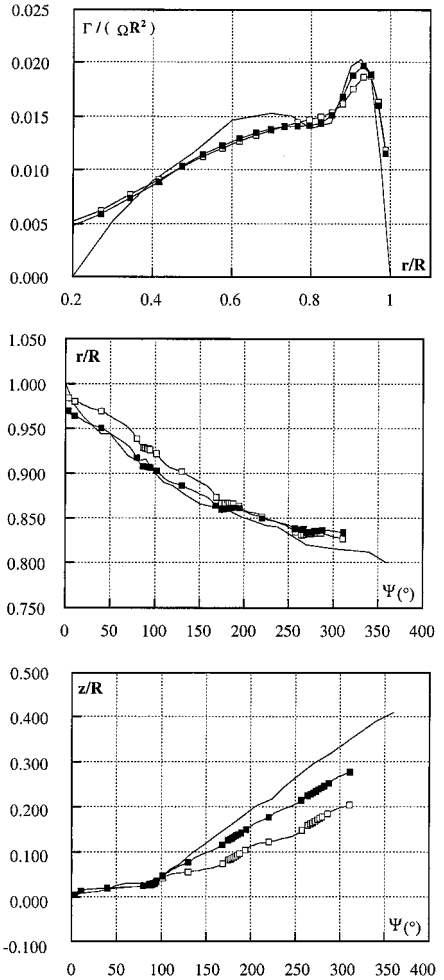


**Fig. 10 Circulation distribution, and radial and axial convection of the tip vortex: rotor ASI 7, four blades, and $\theta$ = 10 deg. ——, measurements; □, Phoenix II-MV; and ■, Phoenix II-MVL.**

repeated process of updating the location of markers can propagate errors in their location. This is an extremely significant problem because the algorithm uses the locations to compute vortical velocities.

An uncertainty analysis, based on Ref. 14, was been carried out,[7] which globally shows that numerical results have to be considered with an averaged statistical discrepancy bar of about 4% (overall and local airloads, flowfield velocity, and tip vortex paths). Moreover, comparisons with the experimental data have also given a global view of the consistency of numerical results.

### C. Airloads Numerical Prediction Versus Experiments

The computed results of the Phoenix II-MVL final code version, concerning thrust, power, and the spanwise loads distribution, have been also compared with the test data obtained using the earlier mentioned KME and PME methods. The prediction of this Phoenix II-MVL code has been checked vs experiments performed on the rectangular AFDD rotor (see Table 1), for two collective pitches ($\theta = 6$ and 10 deg) to assess the accuracy of the solutions.

On such a rotor, a typical run requires a mesh of about 240,000 grids points (see Fig. 11) with about 40 iterations and a run time of about 4 h on a Cray YMP. The predicted $CT$ vs $CQ$ are compared to experiments in Fig. 12, and agreement is shown to be good for the two collective pitch values. The overall performance, however, is better predicted at $\theta = 10$ deg.

Figures 13 and 14 concern the total drag coefficient and the induced drag coefficient at different spanwise locations along the blade of the AFDD rotor. Notice that the important part of the induced-drag contribution to the total drag (80%) is correctly predicted by the numerical method.

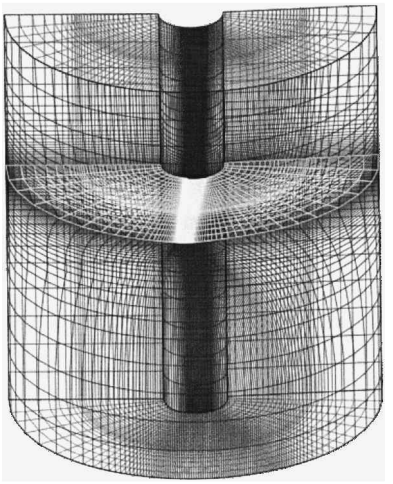

**Fig. 11 Grid topology.**

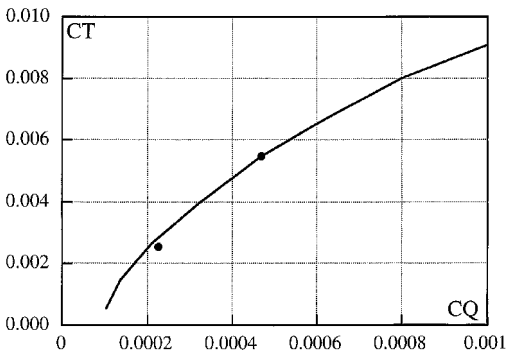


**Fig. 12 Measured and computed rotor thrust and power coefficients: AFDD rotor, $b$ = 2, and rectangular tips. ——, experiment, and ●, Phoenix II-MVL.**

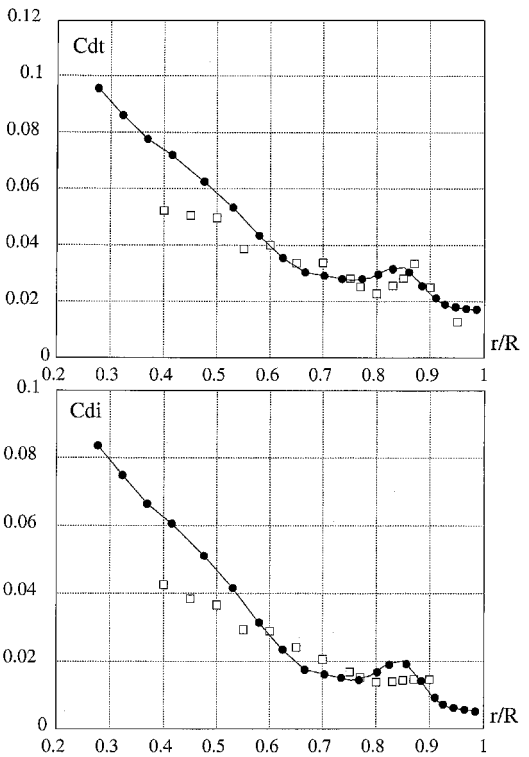


**Fig. 13 Measured and computed total drag coefficient and induced-drag coefficient at different spanwise locations: AFDD rotor, $b$ = 2, and $\theta$ = 6 deg. □, experiment, and ●, Phoenix II.**

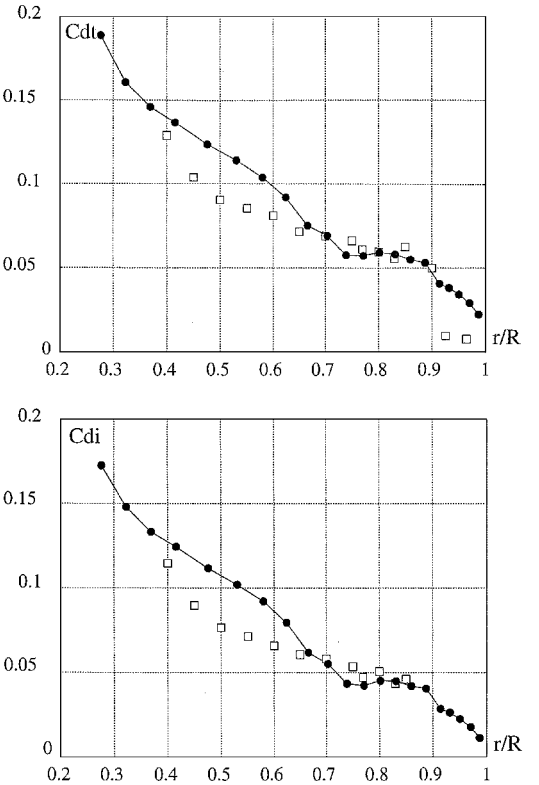


**Fig. 14 Measured and computed total drag coefficient and induced-drag coefficient at different spanwise locations: AFDD rotor, $b$ = 2, and $\theta$ = 10 deg. □, experiment, and ●, Phoenix II.**

For the case corresponding to the collective pitch $\theta = 6$ deg (Fig. 13), the computed results are shown to be in good agreement with the experiments, especially for spanwise sections located between $r/R = 0.6$ and $r/R = 1$. On the other hand, there is a trend to overpredict the drag near the root blade. It is shown that the experimental peak at the location $r/R = 0.85$, due to the tip vortex interaction, is also correctly matched by the calculation method. The same remarks stand for the 10-deg collective pitch value (Fig. 14). Also notice that the spanwise position and the amplitude of the $Cdi$ kink observed near $r/R \approx 0.8$ are better predicted by calculation in this case.

## V. Conclusions

A numerical and experimental investigation of the drag mechanisms of a helicopter rotor in hover is described. The experimental approach, conducted by means of overall and local measurements, focused on determining the three-dimensional velocity field around the blade and in its wake using an LV methodology and contributed to improving the VE full potential method.

From the present results it is shown that the new Phoenix II-MVL code version appears efficient to perform complete performance computations. Among the different improvements given to this numerical method, the most significant concerns the accuracy improvement of the wake geometry and tip vortex trajectory prediction. The main effect of this change is an improvement of the vortex radial location that provided an improved overall loading and power prediction. The present results also indicate good agreement with experimental data for the induced and total drag coefficient along the blade span.

Although the present Phoenix II-MVL code version still requires further validation studies and comparisons with additional overall and local databases, it appears to be an efficient design tool for rotor blades in the hovering flight configuration.

## Acknowledgments

The authors wish to thank the support provided by the Délégation Générale de l'Armement under Grants 92/061 and 9691/022. The

authors would also like to acknowledge John Steinhoff for his valuable suggestions throughout the course of this work.

## References

[1]Silva, M., Favier, D., Ramos, J., Nsi Mba, M., and Berton, E., "An Experimental Investigation of the Drag Mechanisms of a Helicopter Rotor in Hovering Flight," 19th European Rotorcraft Forum, Associazone Italiana di Aeronautica ed Astronautica, Paper 18, Cernobbio, Italy, Sept. 1993.

[2]Ramos, J., Nsi Mba, M., Berton, E., Favier, D., and Silva, M., "A Laser Velocimetric Investigation of the Airloads and Performance of a Model Helicopter Rotor in Hover," *American Helicopter Society*, Aeromechanics Specialists Conf., Paper 8, San Francisco, CA, Jan. 1994.

[3]Berton, E., Favier, D., Maresca, C., and Nsi Mba, M., "Airloads Determination on the Hovering Rotor Using a Laser Velocimetry Technique," CP-552, AGARD, Vol. 1, No. 24, 1995, pp. 24-1–24-6.

[4]Steinhoff, J., and Ramachandran, K., "Free Wake Analysis of Compressible Rotor Flows Fields in Hover," 12th European Rotorcraft Forum, Paper 20, DGLR, Garmish, Germany, Sept. 1986.

[5]Tung, C., and Lee, S., "Evaluation of Hover Performance Prediction Codes," *Proceedings of the American Helicopter Society 50th Annual Forum*, Vol. 2, American Helicopter Society, Washington, DC, 1994, pp. 829–845.

[6]Ramachandran, K., Moffit, R. C., Owen, S. J., and Caradonna, F. X., "Evaluation of Hover Performance Prediction Codes," *Proceedings of the American Helicopter Society 50th Annual Forum*, Vol. 2, American Helicopter Society, Washington, DC, 1994, pp. 1259–1274.

[7]Del Bianco, P., "Contribution à l'Etude Numérique de l'Aérodynamique d'un Rotor par une Méthode de Type Potentiel Complet-Validation en Vol Stationnaire par Comparaison avec l'Expérience," Ph.D. Dissertation, Univ. of Aix–Marseille II, IRPHE/ASI Inst., Marseilles, France, Oct. 1996.

[8]Del Bianco, P., Berton, E., Favier, D., Maresca, C., Yonghu, W., and Steinhoff, J., "Flow Field Prediction for Helicopter Rotor in Hover Using a Vortex Embedding Method," *Proceedings of the 23rd European Rotorcraft Forum*, Vol. 1, DGLR, Dresden, Germany, 1997, pp. 3.1–3.10.

[9]Moulton, M. A., Yonghu, W., and Caradonna, F. X., "Free-Wake Hover Flow Prediction with a Hybrid Potential/Navier–Stokes Solver," *Proceedings of the American Helicopter Society 55th Annual Forum*, American Helicopter Society, Paper E-5, Montreal, Canada, 1999.

[10]Ramos, J., Favier, D., Berton, E., and Nsi Mba, M., "Laser Velocimetry Method Applied to Induced Drag Determination on Hovering Rotor Blades," *Proceedings of the 14th AIAA Applied Aerodynamics Conference*, AIAA Paper 96-2415, Pt. 1, New Orleans, LA, 1996, pp. 322–330.

[11]Ramos, J., Nsi Mba, M., Favier, D., and Berton, E., "Near Wake L. V. Investigation on Hovering Rotor Blades," *Proceedings of the 8th International Symposium on Applications of Laser Techniques to Fluid Mechanics*, Instituto Superior Tecnico, Lisboa, Portugal, 1996, pp. 141.1–141.8.

[12]Wake, B. E., and Baeder, J. D., "Evaluation of a Navier–Stokes Analysis Method for Hover Performance Prediction," *Journal of the American Helicopter Society*, Vol. 41, No. 1, 1996. pp. 7–17.

[13]Beaumier, P., Zibi, J., and Costes, M., "CFD Drag and Power Prediction for a Rotor in Hover or Forward Flight. Formulation and First Applications," *Journal of the American Helicopter Society*, Vol. 42, No. 4, 1997, pp. 327–336.

[14]Jameson, A., and Martinelli, L., "Mesh Refinement and Modelling Errors in Flow Simulation," *AIAA Journal*, Vol. 36, No. 5, 1998, pp. 676–686.